# Magnetic and Multiferroic Properties of Two-Dimensional FePX$_3$ and CuFeP$_2$X$_6$ (X = S, Se, and Te)

Qingyang Wang, Mengmeng Niu, Weikang Zhou, Yicheng Ma, Chun Huang, Gege Yang, Yan Shao, Xu Wu, Cong Wang, Wei Ji,* Yeliang Wang,* and Jingsi Qiao*

ACCESS | Metrics & More | Article Recommendations | Supporting Information

**ABSTRACT:** Two-dimensional (2D) multiferroic materials have significant application potential for novel storage devices due to their tunable magnetic and ferroelectric properties. Transition metal phosphorus chalcogenides MPX$_3$ (X = S, Se, and Te) were found to be magnetic and multiferroic with excellent tunability, promising for multifunctionalized applications. In this study, we investigated the antiferromagnetic and antiferroelectric properties of two-dimensional FePX$_3$ and CuFeP$_2$X$_6$ by density functional theory. Monolayer FePS$_3$/FePSe$_3$ and FePTe$_3$ take intralayer zigzag and Neel antiferromagnetic ground states, respectively. This tunability of intralayer magnetism results from the competition between the spin-exchange interactions of the first and second nearest Fe atoms. Bilayer FePX$_3$ shows weak interlayer interactions and keeps electronic and magnetic characteristics similar to those of the monolayer. Moreover, by introducing the nonmagnetic Cu atom into FePX$_3$, the inversion symmetry broken induces CuFeP$_2$X$_6$ to be multiferroic materials. The transition barrier between ferroelectric (FE) and antiferroelectric (AFE) phases in CuFeP$_2$S$_6$ and CuFeP$_2$Se$_6$ is 0.09 and 0.04 eV/f.u., similar to well-known multiferroic CuCrP$_2$S$_6$. FE-to-AFE phase transition is expected to be achieved by applying an electric field and uniaxial strain. CuFeP$_2$Te$_6$ shows the ground state with a distorted paraelectric phase. Our results show the fundamental properties and in-depth understanding of 2D FePX$_3$ and CuFeP$_2$X$_6$, guiding further investigation of 2D multifunctionalized magnetoelectric devices.

**KEYWORDS:** 2D magnetic materials, DFT calculation, FePX$_3$, antiferroelectricity, multiferroic
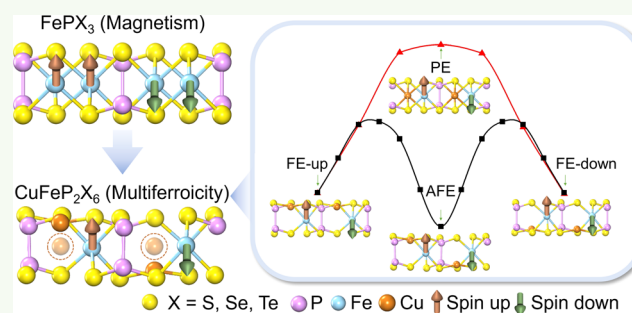
## INTRODUCTION

Materials with spin or electric polarization are promising for application in ultralow power storage devices.[1−4] Particularly, multiferroic materials that exhibit magnetoelectronic coupling interaction exhibit better performance for multifunctionalized electronic devices. Therein, partial layered materials can maintain their multiferroic properties to the two-dimensional (2D) limit, accompanied by the characteristics of 2D materials: atomic layer thickness, abundant interface, and more flexible tunability than bulk materials.[5−8] 2D multiferroic materials are attracting much attention. 2D transition metal phosphorus chalcogenides MPX$_3$ (M = Mn, Fe, Ni, etc.; X = S, Se, and Te) show abundant magnetic properties.[9−17] Meanwhile, ferroelectricity could be induced into MPX$_3$ by the substitution of metal atoms. For instance, multiferroic CuCrP$_2$S$_6$[18] displays tunable ferroelectricity and is a candidate for magnetoelectric memory.[19] Two different types of ferroelectric phases of CuVP$_2$S$_6$ take FM and AFM orders, respectively, exhibiting a strong coupling between electric and magnetic polarization.[20] 2D MNP$_2$X$_6$ multiferroic system widely broadens the application prospect.[21,22]

A representative MPX$_3$, FePS$_3$ is a charge-transfer insulator with Mott insulating,[23,24] has been verified as Ising-type[10,25]

antiferromagnetic material and persists down to the monolayer limit.[26] In detail, FePS$_3$ exhibits intralayer zigzag antiferromagnetic order and interlayer AFM configuration[27,28] with Neel temperature at ~118 K.[10] The magnetic order of FePS$_3$ could induce anisotropy accompanying structural distortion.[26] It is still under debate whether the thickness of the material influences the magnetic properties.[28−30] The magnetic and fundamental properties of the FePX$_3$ family need to be uncovered. Besides, when Cu substitution was brought into the FePX$_3$ family to break the inversion symmetry, ferroelectric properties may be introduced into the magnetic CuFeP$_2$X$_6$ system. The multiferroic properties of CuFeP$_2$X$_6$ systems require further investigation.

In this work, we systematically investigate the magnetic and ferroelectric properties of 2D FePX$_3$ and CuFeP$_2$X$_6$ (X = S, Se, and Te) by density functional theory. FePX$_3$ is a charge-
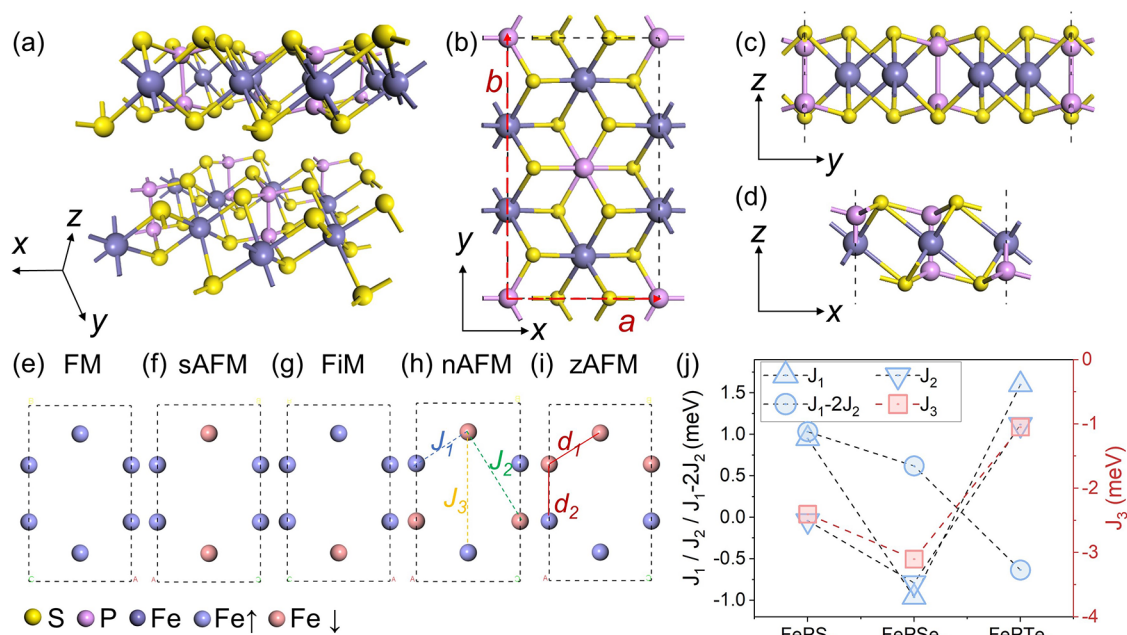
A

**Figure 1.** (a) Atomic structure of bilayer $FePS_3$ in perspective views. Atomic structures of monolayer $FePS_3$ in top view (b) and side views (c, d). Yellow, light purple, and dark purple balls represent S, P, and Fe atoms, respectively. Red dotted lines labeled in (b) are the $a$ and $b$ axes. (e−i) Five magnetic configurations of FM, stripe AFM (sAFM), ferrimagnetic (FiM), Neel AFM (nAFM), and zigzag AFM (zAFM). $J_1$–$J_3$ are the first, second, and third nearest Fe−Fe spin-exchange parameters. $d_1$ and $d_2$ represent the distances between the two Fe atoms. Purple (pink) balls represent spin-up (down) Fe atoms. (j) Spin-exchange parameters of monolayer $FePX_3$.

transfer insulator. Monolayer $FePS_3$ and $FePSe_3$ take zigzag antiferromagnetic (AFM) order, while $FePTe_3$ takes Neel AFM. Monolayer and bilayer $FePS_3$ show direct bandgaps (∼1.6 eV), while the bandgaps of $FePSe_3$ and $FePTe_3$ are indirect and dramatically decrease compared to $FePS_3$. Bilayer $FePS_3$ prefers $C2/m$ phase, and $FePSe_3/FePTe_3$ take $R\overline{3}$ phases. Moreover, we provide an in-depth understanding of multiferroic $CuFeP_2X_6$. We found the AFE-to-FE phase transition is expected to be achieved by applying an electric field and uniaxial strain. This work is meaningful for understanding the magnetic and ferroelectric properties of $FePX_3$ and $CuFeP_2X_6$, and it may promote the discovery of more possible candidates for 2D multiferroic material.

## METHODS

Density functional theory (DFT) calculations were performed using the generalized gradient approximation (GGA) for the exchange-correlation potential, the projector augmented wave (PAW) method,[31,32] and a plane-wave basis set as implemented in the Vienna Ab initio Simulation Package (VASP).[33,34] $1 \times \sqrt{3}$ or $2 \times \sqrt{3}$ orthorhombic supercells of monolayer and bilayer $FePX_3$ were adopted to explore the seven intralayer magnetic configurations. Dispersion corrections were considered at the DFT-D3 level with the Perdew−Burke−Ernzerhof (PBE) functional.[35,36] A $10 \times 6 \times 1$ $k$-mesh was used to sample the first Brillouin zone. A sufficiently large vacuum layer over 18 Å along the out-of-plane direction was adopted. The kinetic energy cutoff for the plane-wave basis was set to 700 eV for the geometric properties and electronic structures calculation. In structural relaxations, all atoms were fully relaxed until the residual force on every atom was less than 0.005 eV·Å$^{-1}$ and reached the energy convergence criteria of $1 \times 10^{-6}$ eV. On-site Coulomb interactions were considered on the Fe d orbitals with an effective value $U = 3$ eV.

The in-plane strain was defined as

$$\varepsilon = \frac{a - a_0}{a_0} \times 100\%$$

where $a_0$ and $a$ denote lattice constants before and after applying in-plane strain.

The differential charge density was derived by

$$\Delta\rho_d = \rho_0 - \rho_{up} - \rho_{dn}$$

$\rho_0$ is the charge density of bilayer $FePX_3$. $\rho_{up}$ and $\rho_{dn}$ are the charge densities of the upper and lower layers of bilayer $FePX_3$.

The phonon spectra were calculated using the finite difference method.[37] The phonon dispersions of $CuFeP_2S_6$ were corrected by hiPhive with the correction of Born−Huang rotational invariance.[38] The error caused by different supercells is considered. The climbing image nudged elastic band (CI-NEB) method[39] is used to determine the energy barriers of the various kinetic processes.

## RESULTS AND DISCUSSION

For monolayer $FePX_3$ (X = S, Se, Te), transition metal magnetic atom Fe is surrounded by 6 chalcogenide atoms and connected by P−P bonds perpendicular to the out-of-plane direction (Figures 1a−d and S1). $1 \times \sqrt{3}$ and $2 \times \sqrt{3}$ orthorhombic supercells were adopted to consider seven magnetic configurations, including FM (Figure 1e), stripe AFM (sAFM) (Figure 1f), ferrimagnetic (FiM) (Figure 1g), Neel AFM (nAFM) (Figure 1h), zigzag AFM (zAFM) (Figure 1i), armchair AFM (Figure S2f), and armchair-fim AFM (Figure S2g). Table S1 shows the energy differences among these magnetic configurations. With the atomic number of X atoms increasing, intralayer magnetic ground states transfer from the zAFM of $FePS_3$ and $FePSe_3$ to the nAFM of $FePTe_3$. The energy differences per Fe atom between zAFM and nAFM are 8, 5, and −5 meV in $FePS_3$, $FePSe_3$, and $FePTe_3$, respectively. Meanwhile, the lattice parameters increase with the chalcogenide atom number. The lattice constants of zAFM $FePS_3$, zAFM $FePSe_3$, and nAFM $FePTe_3$ are $a = 5.98$ Å/$b =$ 10.30 Å, $a = 6.31$ Å/$b = 10.85$ Å, and $a = 6.76$ Å/$b = 10.82$ Å, respectively. We observed that the antiferromagnetic orders
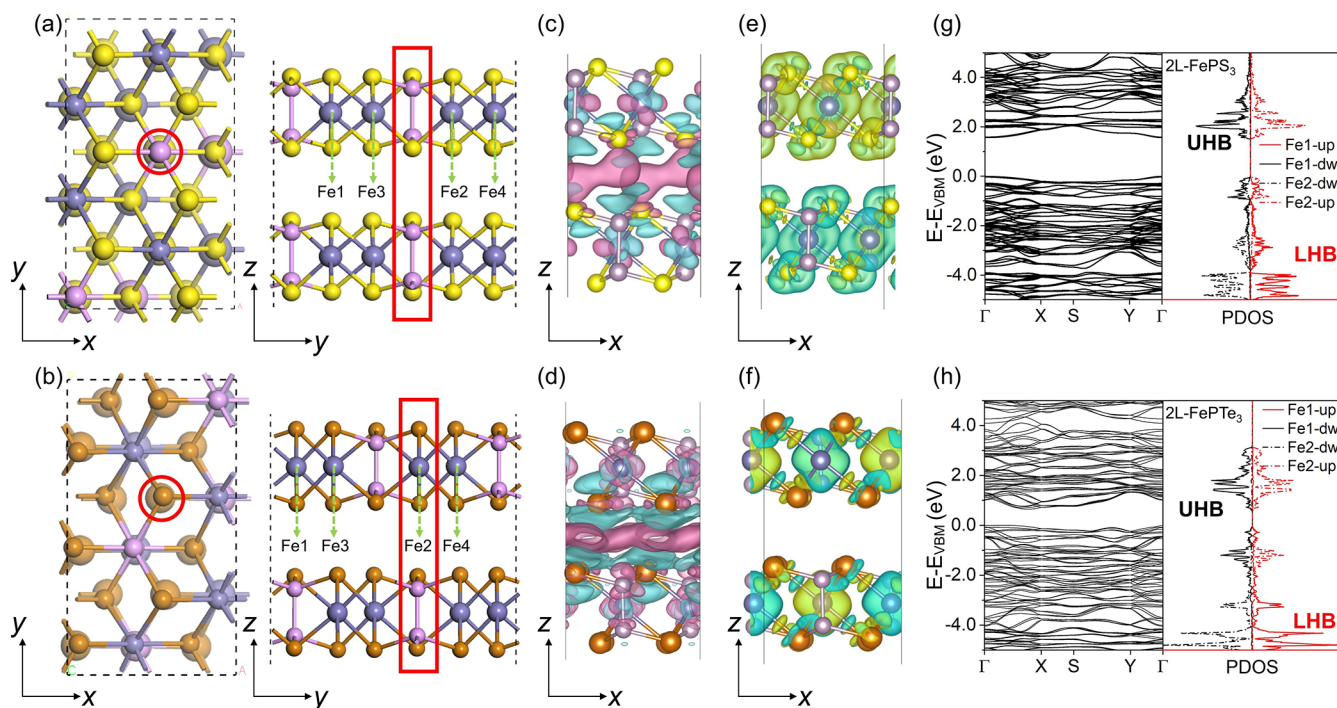
**Figure 2.** (a, b) Bilayer $C2/m$ phase $FePS_3$ and $R\bar{3}$-phase $FePTe_3$ in the top and side views, respectively. (c, d) Differential charge density of bilayer $FePS_3$ and $FePTe_3$. Pink and blue isosurfaces indicate charge accumulation and depletion, respectively. The isosurface value is $1 \times 10^{-4}$ e/Bohr³. Spin densities of bilayer inter-AFM $FePS_3$ (e) and inter-FM $FePTe_3$ (f). The yellow and green regions represent positive and negative charge distributions. The isosurface value is $1 \times 10^{-3}$ e/Bohr³. (g, h) Band structures and projected density of states (PDOS) on Fe1 and Fe2 atoms (Fe1 = Fe3, Fe2 = Fe4) of bilayer $FePS_3$ and $FePTe_3$.

induce anisotropy of the geometric structures. For zAFM configurations, the distances between adjacent Fe atoms show an ~5% difference along and perpendicular to the zigzag magnetic order direction. nAFM $FePTe_3$ shows the largest lattice anisotropy. In detail, the Fe−Fe interatomic distances of $d_1/d_2$ (Figure 1i) are 3.51/3.33 Å, 3.70/3.50 Å, and 3.83/4.12 Å for $FePS_3$, $FePSe_3$, and $FePTe_3$, respectively. $FePTe_3$ is an essential member of the $FePX_3$ family, but it has not been successfully synthesized experimentally due to the difficulty of synthesizing Te compounds. To verify the stability in theory, we calculated the phonon dispersion of $FePTe_3$. As shown in Figure S3, no imaginary frequencies appear, indicating the stability of $FePTe_3$. $FePTe_3$ is promising to be synthesized experimentally.

We further calculated the intralayer spin-exchange parameters to understand the magnetic properties and the magnetic order transition. As illustrated in Figure 1h, $J_n$ ($n$ = 1, 2, 3) indicates spin-exchange parameters of Fe−Fe with the nearest to farest distances. Each system's four most stable magnetic configurations are selected for $J$ calculation. A Heisenberg model including $J_n$ was adopted to express the total energy of different magnetic configurations as shown in Formulas S1−S7. The models of FM, nAFM, and zAFM configurations reveal that $J_1-2J_2$ and $J_3$ play an important role in magnetic order for $FePX_3$, as shown in Figure 1j. We found that $J_3$ is in the range of −1 to −3 meV, and $J_3$ is more prominent than $J_1-2J_2$. The $J_3$ spin-exchange interaction determined the AFM magnetic ground states of $FePX_3$. The competition between $J_1$ and $J_2$ leads to the transformation from zAFM in $FePS_3$/$FePSe_3$ to nAFM in $FePTe_3$ (Figure 1j). $J_1$ involves a direct exchange interaction between Fe−Fe atoms and super-exchange interaction through the Fe−S−Fe chain. $J_2$ only

includes bi-superexchange interaction. Consequently, as the atomic number of the X atoms increases, the Fe−Fe distance elongates and $J_1-2J_2$ exhibits a rapid decrease, ultimately leading to the intralayer magnetic ground state transition.

We further investigated the magnetic properties of bilayer $FePX_3$. Bulk $FePS_3$ and $FePSe_3$ take two representative phases, $C2/m$[40] and $R\bar{3}$,[27] respectively. For $C2/m$ phase, as shown in the red circle and rectangle in Figure 2a, the S atom of the lower layer aligns with a P atom of the upper layer. The S atom of the lower layer aligns with another S atom at the adjacent layer, corresponding to the $R\bar{3}$ phase in Figure 2b. Bilayer $FePTe_3$ with these two phases were considered. The energy difference between $C2/m$ and $R\bar{3}$ for $FePTe_3$ is 0.061 eV per 1 × √3 supercell. Bilayer $FePS_3$ and $FePSe_3$/$FePTe_3$ take the most stable $C2/m$ and $R\bar{3}$ phase, respectively (Figure S4). Though they show distinct phases, the distance between interlayer adjacent atoms is >3.8 Å, exhibiting a weak interlayer coupling in $FePX_3$. With the atomic number of X atoms increasing, the interlayer X-X interaction becomes slightly stronger, leading $FePSe_3$ and $FePTe_3$ to be the $R\bar{3}$ ground state, which involves more X-X interactions compared to $C2/m$ phases, according to Figure 2c,d.

Next, we analyzed the effect of phase on the magnetic and electronic properties of the bilayer $FePX_3$. Intralayer zAFM/nAFM/FM/sAFM and interlayer FM/AFM magnetic configurations were considered (Table S2). We found that the energy differences between interlayer magnetic orders are 0.03−37.69 meV per Fe atom. The interlayer magnetic order transfers from the interlayer AFM of $FePS_3$ (Figure 2a) to FM of $FePTe_3$ (Figure 2b). The intralayer magnetic order remains zAFM (Figure 2e) or nAFM (Figure 2f), the same as that of monolayer $FePX_3$. Besides, bilayer $FePX_3$ shows similar
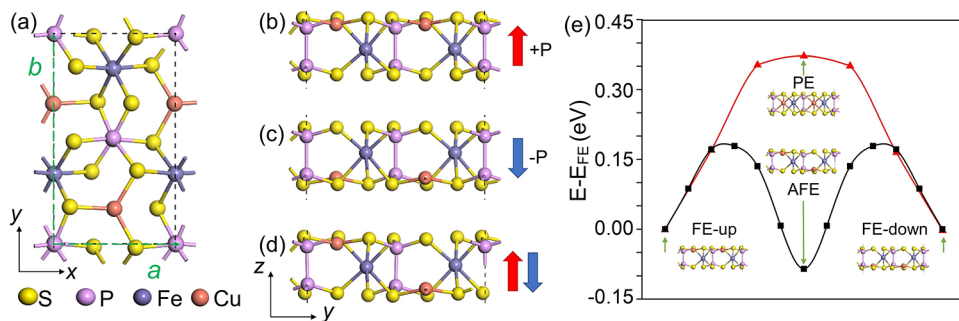
**Figure 3.** (a−d) Atomic structure of monolayer $CuFeP_2S_6$ in top view (a) and side view for ferroelectric-up (b) and ferroelectric-down (c) and antiferroelectric (d) phases. (e) Kinetic pathways of phase transitions among different FE and AFE $CuFeP_2S_6$. The pathways of the red and black lines are FE-up-PE-FE-down and FE-up-AFE-FE-down, respectively.
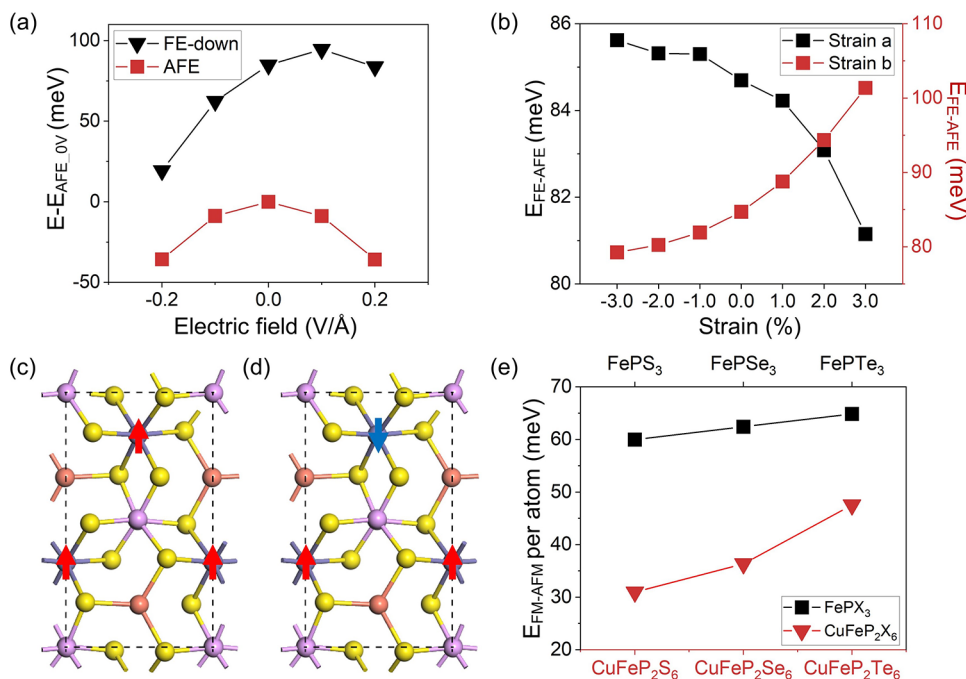


**Figure 4.** (a) Energy evolution of FE and AFE $CuFeP_2S_6$ by an electric field. The energy of the AFE $CuFeP_2S_6$ ground state is set at 0 eV. (b) Energy difference between FE $CuFeP_2S_6$ and AFE $CuFeP_2S_6$ ($E_{FE-AFE}$) under uniaxial strain in the $a(x)$ axis (black line) and $b(y)$ axis (red line). (c, d) Configurations of intralayer FM (c) and AFM (d) $CuFeP_2S_6$ in top views. (e) Energy difference per Fe atom between FM and AFM for $FePX_3$ (black line) and $CuFeP_2X_6$ (red line).

electronic bandgap and characteristics to monolayer ones, as shown in the band structure (Figure S5) and total density of states (DOS) (Figure S6). The upper and lower layers of $FePX_3$ show similar projected DOS on Fe atoms (PDOS) features. The PDOS of the upper layer $FePX_3$ is shown in Figures 2g,h, S7, and S8. $FePS_3$ and $FePSe_3$ show Mott insulating in recent experimental and theoretical results.[23,24] $FePS_3$, $FePSe_3$ and $FePTe_3$ are charge-transfer insulators, with a larger Mott gap than the bandgap. The upper and lower Hubbard bands are mainly contributed by the d orbital of Fe atoms according to PDOS (Figures S7 and S8). The direct bandgaps of monolayer and bilayer $FePS_3$ are both 1.57 eV at the Γ point (Figure 2g). The bandgaps of monolayer and bilayer $FePSe_3/FePTe_3$ are indirect and decrease to 1.44/0.61 eV (Figures S5e and 2h), respectively. Monolayer and bilayer bandgaps are similar to the bulk ones,[38,40] indicating the weak interlayer coupling effect on the electronic properties in $FePX_3$.

Introducing Cu atoms into $FePX_3$ breaks the inversion symmetry and is expected to introduce ferroelectricity.

$MNP_2X_6$ family, e.g., $CuNP_2S_6$ (N = Cr, In, V), are significant candidates for 2D ferroelectric materials. Analogously, we constructed a monolayer $CuFeP_2X_6$ unit cell by replacing 2 Fe atoms with 2 Cu atoms in $1 \times \sqrt{3}$ $FePX_3$ supercell, as shown in Figure 3a−d. Cu substitution induces that lattice constants of $CuFeP_2S_6$ expanded to $a$ = 6.01 Å and $b$ = 10.40 Å from those of $FePS_3$ ($a$ = 5.98 Å, $b$ = 10.30 Å). Similar to $CuCrP_2S_6$,[41] total DOS and PDOS (Figures S9−S11) indicate that $CuFeP_2X_6$ show Mott insulating, corresponding to charge-transfer insulators. The bandgaps of monolayer $CuFeP_2S_6$, $CuFeP_2Se_6$, and $CuFeP_2Te_6$ are 0.88, 0.81, and 0.45 eV, respectively. The Cu atoms shift along the out-of-plane direction, which could induce different electric polarization. Figure 3b,c shows that when two Cu atoms are located at the upper or lower sublayer of $CuFeP_2S_6$, forming FE phases, the direction of the dipole moment is along $+z$ and $−z$, respectively. The dipole moments of monolayer FE $CuFeP_2X_6$ (X = S, Se, Te) are 0.55, 0.33, and 0.28 pC/m, respectively. The dipole moment of $CuFeP_2X_6$ decreased with the atomic

number of X atom increasing and is at the same order of magnitude with 0.6−0.8 pC/m of monolayer $CuCrP_2S_6$, $CuCrP_2Se_6$, $CuVP_2S_6$, and $CuVP_2Se_6$.[42]

When two Cu atoms are located at different sublayers in Figure 3d, no net dipole moment remains, leading to the AFE phase. AFE phases are 0.085, 0.077, and 0.058 eV more stable than the FE phases of $CuFeP_2X_6$, respectively. $CuFeP_2S_6$ and $CuFeP_2Se_6$ take AFE ground states (Figure S12). However, the ground state of $CuFeP_2Te_6$ is a distorted PE (paraelectric) phase (Figure S13). Cu atoms bond with four surrounding Te atoms rather than six Te atoms. We also calculated the phonon dispersion of $CuFeP_2S_6$. As shown in Figure S14, no imaginary frequencies appear, indicating the stability of $CuFeP_2S_6$. To confirm the ferroelectricity of $CuFeP_2S_6$ (Figure 3e) and $CuFeP_2Se_6$ (Figure S15b), we calculated the transition barrier between two FE configurations with opposite polarization directions and between FE and AFE configurations using the climbing image nudged elastic band (CI-NEB) method. Figure 3e shows two possible transition pathways from the FE-up to FE-down phase of $CuFeP_2S_6$. The PE pathway should overcome ~0.37 eV barrier per unit cell (~0.19 eV/f.u.). Moreover, the transition barrier from FE to AFE is about 0.18 eV per unit cell (0.09 eV/f.u.) for $CuFeP_2S_6$ $CuFeP_2Se_6$, and 0.08 eV per unit cell (0.04 eV/f.u.) for $CuFeP_2Se_6$. These barriers are smaller than that of $CuInP_2S_6$ and similar to that of $CuCrP_2S_6$.[19,43]

We investigated the electric field and strain effect on manipulating the ferroelectricity of monolayer $CuFeP_2X_6$. Figure 4a shows the variation of the energy difference between the FE and AFE ($E_{FE-AFE}$) for monolayer $CuFeP_2S_6$ when an out-of-plane electric field is applied. For the ferroelectric polarization state, a negative electric field, the same as the direction of the dipole moment in the FE phase, could effectively reduce the $E_{FE-AFE}$, promoting the phase transition between the FE and AFE. A positive electric field in the dipole moment's opposite direction will suppress the phase transition. Furthermore, the uniaxial strain along the $a$ or $b$ axis was applied to $CuFeP_2S_6$ to modulate $E_{FE-AFE}$, respectively (Figure 4b). It was found that tensile and compressive strain along the $a$ or $b$ axis could decrease and increase the $E_{FE-AFE}$, which is also a means to manipulate the ferroelectricity. Similar behavior has also been noted in $CuFeP_2Se_6$ (Figure S16). These findings may provide guidance and information for future explorations of the two-dimensional ferroelectric family.

Moreover, the magnetic ground states of the monolayer $CuFeP_2S_6$ were studied by considering FM (Figure 4c) and nAFM (Figure 4d) configurations. nAFM magnetic order is magnetic ground state in both FE and AFE phases, which is robust enough, but it is challenging to switch the magnetic order. Compared with $FePX_3$, the Cu atom replacement also influences magnetization. For example, the energy difference between FM and AFM in $CuFeP_2S_6$ is around 30 meV per Fe atom, which is lower than 60 meV in $FePS_3$ (Figure 4e). Although introducing nonmagnetic Cu atoms disrupts the first and third nearest-neighbor exchange interactions in $FePX_3$, the magnetic moment per Fe atom increased from 3.56 $\mu_B$ ($FePS_3$) to 3.83 $\mu_B$ ($CuFeP_2S_6$), 3.53 $\mu_B$ ($FePSe_3$) to 3.76 $\mu_B$ ($CuFeP_2Se_6$), and 3.45 $\mu_B$ ($FePTe_3$) to 3.62 $\mu_B$ ($CuFeP_2Te_6$). $CuFeP_2S_6$ coexists with magnetic properties and ferroelectricity. The multiferroic properties of $CuFeP_2S_6$ make it promising for application in the storage field.

## CONCLUSIONS

In this work, we investigated the magnetic and electronic properties of 2D $FePX_3$ (X = S, Se, Te) by first-principles calculations. 2D $FePX_3$ exhibits intralayer antiferromagnetic ground states and weak interlayer coupling. To further explore the $FePX_3$ family, we replace half of the Fe atoms with Cu atoms and analyze the ferroelectric properties of the monolayer $CuFeP_2X_6$ material. $CuFeP_2S_6$ and $CuFeP_2Se_6$ take the AFE ground state. However, the ground state of $CuFeP_2Te_6$ is a distorted PE phase. The electric field in the same direction of the dipole moment and uniaxial tensile strain could decrease the energy difference between AFE and FE, promoting the phase transition between AFE and FE. These results provide an in-depth understanding and analysis of the magnetic properties of $FePX_3$ and multiferroic properties of $CuFeP_2X_6$, facilitating the exploration of the 2D multiferroic family.

## ASSOCIATED CONTENT

### Ⓢ Supporting Information

The Supporting Information is available free of charge at https://pubs.acs.org/doi/10.1021/acsaelm.4c01547.

Atomic structure of all materials mentioned in the manuscript; seven magnetic configurations and their energies of monolayer $FePX_3$; phonon dispersions of monolayer $FePTe_3$ and $CuFeP_2S_6$; band structures and density of states; transition pathways of FE to AFE in monolayer $CuFeP_2S_6$ and $CuFeP_2Se_6$; energy evolution of FE and AFE $CuFeP_2S_6$ and $CuFeP_2Se_6$ under electric field and uniaxial strain; and Heisenberg model including the nearest spin-exchange parameters. (PDF)

## AUTHOR INFORMATION

### Corresponding Authors

**Wei Ji** − *Beijing Key Laboratory of Optoelectronic Functional Materials & Micro-Nano Devices, Department of Physics, Renmin University of China, Beijing 100872, China;* ⓘ orcid.org/0000-0001-5249-6624; Email: wji@ruc.edu.cn

**Yeliang Wang** − *School of Integrated Circuits and Electronics & Advanced Research Institute of Multidisciplinary Science, Beijing Institute of Technology, Beijing 100081, China;* ⓘ orcid.org/0000-0002-8896-0748; Email: yeliang.wang@bit.edu.cn

**Jingsi Qiao** − *School of Integrated Circuits and Electronics & Advanced Research Institute of Multidisciplinary Science, Beijing Institute of Technology, Beijing 100081, China;* ⓘ orcid.org/0000-0001-6464-5500; Email: qiaojs@bit.edu.cn

### Authors

**Qingyang Wang** − *School of Integrated Circuits and Electronics & Advanced Research Institute of Multidisciplinary Science, Beijing Institute of Technology, Beijing 100081, China*

**Mengmeng Niu** − *School of Integrated Circuits and Electronics & Advanced Research Institute of Multidisciplinary Science, Beijing Institute of Technology, Beijing 100081, China*

**Weikang Zhou** − *School of Integrated Circuits and Electronics & Advanced Research Institute of Multidisciplinary Science, Beijing Institute of Technology, Beijing 100081, China*

**Yicheng Ma** − *School of Integrated Circuits and Electronics & Advanced Research Institute of Multidisciplinary Science, Beijing Institute of Technology, Beijing 100081, China*

**Chun Huang** − *School of Integrated Circuits and Electronics & Advanced Research Institute of Multidisciplinary Science, Beijing Institute of Technology, Beijing 100081, China*

**Gege Yang** − *School of Integrated Circuits and Electronics & Advanced Research Institute of Multidisciplinary Science, Beijing Institute of Technology, Beijing 100081, China*

**Yan Shao** − *School of Integrated Circuits and Electronics & Advanced Research Institute of Multidisciplinary Science, Beijing Institute of Technology, Beijing 100081, China*

**Xu Wu** − *School of Integrated Circuits and Electronics & Advanced Research Institute of Multidisciplinary Science, Beijing Institute of Technology, Beijing 100081, China;*
ⓘ orcid.org/0000-0002-2252-322X

**Cong Wang** − *Beijing Key Laboratory of Optoelectronic Functional Materials & Micro-Nano Devices, Department of Physics, Renmin University of China, Beijing 100872, China*

Complete contact information is available at:
https://pubs.acs.org/10.1021/acsaelm.4c01547

**Notes**
The authors declare no competing financial interest.

## ■ REFERENCES

(1) Spaldin, N. A.; Ramesh, R. Advances in magnetoelectric multiferroics. *Nat. Mater.* **2019**, *18* (3), 203−212.

(2) Bibes, M.; Barthelemy, A. Multiferroics: towards a magnetoelectric memory. *Nat. Mater.* **2008**, *7* (6), 425−426.

(3) Han, W.; Kawakami, R. K.; Gmitra, M.; Fabian, J. Graphene spintronics. *Nat. Nanotechnol.* **2014**, *9* (10), 794−807.

(4) Ohno, H.; Chiba, D.; Matsukura, F.; Omiya, T.; Abe, E.; Dietl, T.; Ohno, Y.; Ohtani, K. Electric-field control of ferromagnetism. *Nature* **2000**, *408* (6815), 944−946.

(5) Wang, T.; Liu, F.; Liu, S.; Liu, B.; Zhu, S. Interface engineering strategy for multisource spintronic devices via $TMPS_4$ modulation of black-phosphorus. *Phys. Chem. Chem. Phys.* **2023**, *25* (35), 23988−23994.

(6) Guo, Y.; Yu, X.; Zhang, Y.; Zhang, X.; Yuan, S.; Li, Y.; Yang, S. A.; Wang, J. 2D Multiferroicity with Ferroelectric Switching Induced Spin-Constrained Photoelectricity. *ACS Nano* **2022**, *16* (7), 11174−11181.

(7) Tepliakov, N. V.; Ma, R.; Lischner, J.; Kaxiras, E.; Mostofi, A. A.; Pizzochero, M. Dirac Half-Semimetallicity and Antiferromagnetism in Graphene Nanoribbon/Hexagonal Boron Nitride Heterojunctions. *Nano Lett.* **2023**, *23* (14), 6698−6704.

(8) Alliati, I. M.; Evans, R. F. L.; Novoselov, K. S.; Santos, E. J. G. Relativistic domain-wall dynamics in van der Waals antiferromagnet $MnPS_3$. *npj Comput. Mater.* **2022**, *8* (1), No. 3.

(9) Qian, X.; Chen, L.; Yin, L.; Liu, Z.; Pei, S.; Li, F.; Hou, G.; Chen, S.; Song, L.; Thebo, K. H.; Cheng, H. M.; Ren, W. $CdPS_3$ nanosheets-based membrane with high proton conductivity enabled by Cd vacancies. *Science* **2020**, *370* (6516), 596−600.

(10) Nauman, M.; Kiem, D. H.; Lee, S.; Son, S.; Park, J.-G.; Kang, W.; Han, M. J.; Jo, Y. Complete mapping of magnetic anisotropy for prototype Ising van der Waals $FePS_3$. *2D Mater.* **2021**, *8* (3), No. 035011.

(11) Neal, S. N.; Kim, H. S.; O'Neal, K. R.; Haglund, A. V.; Smith, K. A.; Mandrus, D. G.; Bechtel, H. A.; Carr, G. L.; Haule, K.; Vanderbilt, D.; Musfeldt, J. L. Symmetry crossover in layered $MPS_3$ complexes (M = Mn, Fe, Ni) via near-field infrared spectroscopy. *Phys. Rev. B* **2020**, *102* (8), No. 085408.

(12) Du, K. Z.; Wang, X. Z.; Liu, Y.; Hu, P.; Utama, M. I.; Gan, C. K.; Xiong, Q.; Kloc, C. Weak Van der Waals Stacking, Wide-Range Band Gap, and Raman Study on Ultrathin Layers of Metal Phosphorus Trichalcogenides. *ACS Nano* **2016**, *10* (2), 1738−1743.

(13) Kargar, F.; Coleman, E. A.; Ghosh, S.; Lee, J.; Gomez, M. J.; Liu, Y.; Magana, A. S.; Barani, Z.; Mohammadzadeh, A.; Debnath, B.; Wilson, R. B.; Lake, R. K.; Balandin, A. A. Phonon and Thermal Properties of Quasi-Two-Dimensional $FePS_3$ and $MnPS_3$ Antiferromagnetic Semiconductors. *ACS Nano* **2020**, *14* (2), 2424−2435.

(14) Wang, X.; Cao, J.; Lu, Z.; Cohen, A.; Kitadai, H.; Li, T.; Tan, Q.; Wilson, M.; Lui, C. H.; Smirnov, D.; Sharifzadeh, S.; Ling, X. Spin-induced linear polarization of photoluminescence in antiferromagnetic van der Waals crystals. *Nat. Mater.* **2021**, *20* (7), 964−970.

(15) Wang, X.; Cao, J.; Li, H.; Lu, Z.; Cohen, A.; Haldar, A.; Kitadai, H.; Tan, Q.; Burch, K. S.; Smirnov, D.; Xu, W.; Sharifzadeh, S.; Liang, L.; Ling, X. Electronic Raman scattering in the 2D antiferromagnet $NiPS_3$. *Sci. Adv.* **2022**, *8* (2), No. eabl7707.

(16) Samal, R.; Sanyal, G.; Chakraborty, B.; Rout, C. S. Two-dimensional transition metal phosphorous trichalcogenides ($MPX_3$): a review on emerging trends, current state and future perspectives. *J. Mater. Chem. A* **2021**, *9* (5), 2560−2591.

(17) Koo, H. J.; Kremer, R.; Whangbo, M. H. Unusual Spin Exchanges Mediated by the Molecular Anion $P_2S_6^{4−}$: Theoretical Analyses of the Magnetic Ground States, Magnetic Anisotropy and Spin Exchanges of $MPS_3$ (M = Mn, Fe, Co, Ni). *Molecules* **2021**, *26* (5), No. 1410.

(18) Wang, X.; Shang, Z.; Zhang, C.; Kang, J.; Liu, T.; Wang, X.; Chen, S.; Liu, H.; Tang, W.; Zeng, Y. J.; Guo, J.; Cheng, Z.; Liu, L.; Pan, D.; Tong, S.; Wu, B.; Xie, Y.; Wang, G.; Deng, J.; Zhai, T.; Deng, H. X.; Hong, J.; Zhao, J. Electrical and magnetic anisotropies in van der Waals multiferroic $CuCrP_2S_6$. *Nat. Commun.* **2023**, *14* (1), No. 840.

(19) Lai, Y.; Song, Z.; Wan, Y.; Xue, M.; Wang, C.; Ye, Y.; Dai, L.; Zhang, Z.; Yang, W.; Du, H.; Yang, J. Two-dimensional ferromagnetism and driven ferroelectricity in van der Waals $CuCrP_2S_6$. *Nanoscale* **2019**, *11* (12), 5163−5170.

(20) Duan, X.; Wang, H.; Chen, X.; Qi, J. Multiple polarization phases and strong magnetoelectric coupling in the layered transition metal phosphorus chalcogenides $TMP_2X_6$(T = Cu,Ag;M = Cr,V;X = S,Se) by controlling the interlayer interaction and dimension. *Phys. Rev. B* **2022**, *106* (11), No. 115403.

(21) He, Q.; Belianinov, A.; Dziaugys, A.; Maksymovych, P.; Vysochanskii, Y.; Kalinin, S. V.; Borisevich, A. Y. Antisite defects in layered multiferroic $CuCr_{0.9}In_{0.1}P_2S_6$. *Nanoscale* **2015**, *7* (44), 18579−18583.

(22) Hao, K. R.; Ma, X. Y.; Zhang, Z.; Lyu, H. Y.; Yan, Q. B.; Su, G. Ferroelectric and Room-Temperature Ferromagnetic Semiconductors in the 2D $M_I M_{II} Ge_2X_6$ Family: First-Principles and Machine Learning Investigations. *J. Phys. Chem. Lett.* **2021**, *12* (41), 10040−10051.

(23) Dedkov, Y.; Guo, Y.; Voloshina, E. Progress in the studies of electronic and magnetic properties of layered $MPX_3$ materials (M: transition metal, X: chalcogen). *Electron. Struct.* **2023**, *5* (4), No. 043001.

(24) Jin, Y.; Yan, M.; Kremer, T.; Voloshina, E.; Dedkov, Y. Mott−Hubbard insulating state for the layered van der Waals $FePX_3$ (X: S, Se) as revealed by NEXAFS and resonant photoelectron spectroscopy. *Sci. Rep.* **2022**, *12* (1), No. 735.

(25) Joy, P. A.; Vasudevan, S. Magnetism in the layered transition-metal thiophosphates $MPS_3$ (M = Mn, Fe, and Ni). *Phys. Rev. B* **1992**, *46* (9), 5425−5433.

(26) Lee, J. U.; Lee, S.; Ryoo, J. H.; Kang, S.; Kim, T. Y.; Kim, P.; Park, C. H.; Park, J. G.; Cheong, H. Ising-Type Magnetic Ordering in Atomically Thin $FePS_3$. *Nano Lett.* **2016**, *16* (12), 7433−7438.

(27) Zheng, Y.; Jiang, X.-x.; Xue, X.-x.; Dai, J.; Feng, Y. Ab initio study of pressure-driven phase transition in $FePS_3$ and $FePSe_3$. *Phys. Rev. B* **2019**, *100* (17), No. 174102.

(28) Wang, X.; Du, K.; Fredrik Liu, Y. Y.; Hu, P.; Zhang, J.; Zhang, Q.; Owen, M. H. S.; Lu, X.; Gan, C. K.; Sengupta, P.; Kloc, C.; Xiong, Q. Raman spectroscopy of atomically thin two-dimensional magnetic iron phosphorus trisulfide ($FePS_3$) crystals. *2D Mater.* **2016**, *3* (3), No. 031009.

(29) Kim, T. Y.; Park, C. H. Magnetic Anisotropy and Magnetic Ordering of Transition-Metal Phosphorus Trisulfides. *Nano Lett.* **2021**, *21* (23), 10114−10121.

(30) Martín-Pérez, L.; Medina Rivero, S.; Vazquez Sulleiro, M.; Naranjo, A.; Gomez, I. J.; Ruiz-Gonzalez, M. L.; Castellanos-Gomez, A.; Garcia-Hernandez, M.; Perez, E. M.; Burzuri, E. Direct Magnetic Evidence, Functionalization, and Low-Temperature Magneto-Electron Transport in Liquid-Phase Exfoliated $FePS_3$. *ACS Nano* **2023**, *17* (3), 3007−3018.

(31) Blöchl, P. E. Projector augmented-wave method. *Phys. Rev. B* **1994**, *50* (24), 17953−17979.

(32) Kresse, G.; Joubert, D. From ultrasoft pseudopotentials to the projector augmented-wave method. *Phys. Rev. B* **1999**, *59* (3), 1758−1775.

(33) Kresse, G.; Furthmuller, J. Efficient iterative schemes for ab initio total-energy calculations using a plane-wave basis set. *Phys. Rev. B* **1996**, *54* (16), 11169−11186.

(34) Kresse, G.; Furthmüller, J. Efficiency of ab-initio total energy calculations for metals and semiconductors using a plane-wave basis set. *Comput. Mater. Sci.* **1996**, *6* (1), 15−50.

(35) Grimme, S. Semiempirical GGA-type density functional constructed with a long-range dispersion correction. *J. Comput. Chem.* **2006**, *27* (15), 1787−1799.

(36) Grimme, S.; Antony, J.; Ehrlich, S.; Krieg, H. A consistent and accurate ab initio parametrization of density functional dispersion correction (DFT-D) for the 94 elements H-Pu. *J. Chem. Phys.* **2010**, *132* (15), No. 154104.

(37) Kresse, G; Furthmuller, J; Hafner, J Ab initio Force Constant Approach to Phonon Dispersion Relations of Diamond and Graphite. *Europhysics Letters (EPL)* **1995**, *32* (9), 729−734.

(38) Lin, C.; Poncé, S.; Marzari, N. General invariance and equilibrium conditions for lattice dynamics in 1D, 2D, and 3D materials. *npj Comput. Mater.* **2022**, *8* (1), No. 236.

(39) Henkelman, G.; Uberuaga, B. P.; Jonsson, H. A climbing image nudged elastic band method for finding saddle points and minimum energy paths. *he Journal of Chemical Physics* **2000**, *113* (22), 9901−9904.

(40) Haines, C. R. S.; Coak, M. J.; Wildes, A. R.; Lampronti, G. I.; Liu, C.; Nahai-Williamson, P.; Hamidov, H.; Daisenberger, D.; Saxena, S. S. Pressure-Induced Electronic and Structural Phase Evolution in the van der Waals Compound $FePS_3$. *Phys. Rev. Lett.* **2018**, *121* (26), No. 266801.

(41) Guo, Y.; Yang, J.; Zhou, J.; Zhu, N.; Jin, Y.; Thiele, G.; Preobrajenski, A.; Voloshina, E.; Dedkov, Y. Electronic Correlations in Multiferroic Van der Waals $CuCrP_2S_6$: Insights from X-ray Spectroscopy and DFT. *J. Phys. Chem. C* **2024**, *128* (18), 7830−7839.

(42) Qi, J.; Wang, H.; Chen, X.; Qian, X. Two-dimensional multiferroic semiconductors with coexisting ferroelectricity and ferromagnetism. *Appl. Phys. Lett.* **2018**, *113* (4), No. 043102.

(43) Bai, H.; Li, X.; Pan, H.; He, P.; Xu, Z. A.; Lu, Y. Van der Waals Antiferroelectric Magnetic Tunnel Junction: A First-Principles Study of a $CrSe_2/CuInP_2S_6/CrSe_2$ Junction. *ACS Appl. Mater. Interfaces* **2021**, *13* (50), 60200−60208.